View Article Online
DOI: 10.1039/D0SM01549K

ARTICLE

Not just a fluidifying effect: omega-3 phospholipids induce formation of non-lamellar structures in biomembranes

Received 00th January 20xx,
Accepted 00th January 20xx

DOI: 10.1039/x0xx00000x

Augusta de Santis,[a,b] Giuseppe Vitiello,[b,c] Marie-Sousai Appavou,[d] Ernesto Scoppola,[e] Giovanna Fragneto,[f] Lester C. Barnsley,[d,g] Luke A. Clifton,[h] Maria Francesca Ottaviani,[i] Luigi Paduano,[a,b] Irene Russo Krauss,[*,a,b] Gerardino D'Errico[*,a,b]

The polyunsaturated omega-3 fatty acid docosaHexaenoic Acid (DHA) is found in very high concentration in a few peculiar tissues suggesting it must have a specialized role. DHA was proposed to affect the function of the cell membrane and related proteins through an indirect mechanism of action, based on the DHA-phospholipid effects on the lipid bilayer structure. In this respect, most studies have focused on its influence on lipid-rafts, somehow neglecting the analysis of effects on liquid disordered phases that constitute most of the cell membranes, by reporting in these cases only a general fluidifying effect. Here, by combining Neutron Reflectivity, Cryo-Transmission Electron Microscopy, Small Angle Neutron Scattering, Dynamic Light Scattering and Electron Paramagnetic Resonance spectroscopy, we characterize liquid disordered bilayers formed by the naturally abundant 1-palmitoyl-2-oleyl-*sn*-glycero-3-phosphocholine and different contents of a di-DHA glycero-phosphocholine, 22:6-22:6PC, from both a molecular/microscopic and supramolecular/mesoscopic viewpoint. We show that, below a threshold concentration of about 40% molar percent, incorporation of 22:6-22:6PC in the membrane increases lipid dynamics slightly but sufficiently to promote membrane deformation and increase of multilamellarity. Notably, beyond this threshold, 22:6-22:6PC disfavours formation of lamellar phases, leading to a phase separation consisting mostly of small spherical particles that coexist with a minority portion of a lipid blob with water-filled cavities. Concurrently, from a molecular viewpoint, the polyunsaturated acyl chains tend to fold and expose the termini to the aqueous medium. We propose that this peculiar tendency is a key feature of the DHA-phospholipids making them able to modulate the local morphology of biomembranes.

Introduction

DocosaHexaenoic Acid (DHA) is the longest and most unsaturated omega-3 fatty acid present in the cell membranes, where it is found mainly as acyl chain of phospholipids esterified in the *sn*-2 or in both the *sn*-1-and *sn*-2 glycerol position (DHA-phospholipids). Levels of DHA-phospholipids in biological membranes depend on the tissue. Typical levels are about 5%, but this content may be further enriched by changes in diet.[1, 2] Notably, in some peculiar tissues, such as the rod cell outer segment in retina and the synapses of neural membranes,[3-6] the amount of DHA approaches the 50% of the total membrane fatty acids, at the expenses of other important omega-3 fatty acids, such as eicosapentaenoic acid, that are virtually absent.[7, 8] Moreover, in these cases dipolyene phospholipids are mostly present.[2, 9-11] Such a limited tissue distribution of high DHA levels implies a specialized, even if yet undefined, role for DHA in these cells.[12] In particular, the high content of DHA in the brain suggests a key role for these molecules in the optimal development, maturation and aging of neural structures and networks.[8, 13] Coherently, DHA has been also proposed to exert strong neuroprotective effects[14]. For these reasons a rich research aimed at understanding the molecular bases of DHA beneficial effects has flourished.

Several hypotheses have been proposed to explain the DHA biological and pharmacological roles,[15] including its radical-scavenging and anti-inflammatory action or specific effects of its mediators.[15] Other researchers have invoked an indirect membrane-

---

[a] Department of Chemical Sciences, University of Naples Federico II, Naples, Italy. Email: gderrico@unina.it; Tel. +39-081-674245; email: irene.russokrauss@unina.it; Tel. +39-081-674227
[b] CSGI (Consorzio per lo Sviluppo dei Sistemi a Grande Interfase), Florence, Italy.
[c] Department of Chemical, Materials and Production Engineering, University of Naples Federico II, Naples, Italy.
[d] Jülich Centre for Neutron Science (JCNS) at Heinz Maier-Leibnitz Zentrum (MLZ), Forschungszentrum Jülich GmbH, Garching, Germany
[e] Max Planck Institut für Kolloid und Grenzflächenforschung, Potsdam, Germany
[f] Institut Laue-Langevin (ILL) Grenoble, France
[g] Current address Australian Synchrotron, ANSTO, Clayton, Australia
[h] ISIS Facility, Science and Technology Facilities Council, Rutherford Appleton Laboratory, Harwell Oxford, Didcot OX11 0QX, United Kingdom
[i] Department of Pure and Applied Sciences, University of Urbino, Urbino, Italy

†Electronic Supplementary Information (ESI) available. Parameters derived from EPR spectra simulation, chemical structures of lipids and spin labels used, analysis of Cryo-TEM images, experimental and simulated EPR spectra, NR experimental data, best fitting curves and *SLD* profiles in different solvents, as well as convoluted and deconvoluted volume fraction profiles. See DOI: 10.1039/x0xx00000x

mediated mechanism of action, based on the DHA-phospholipid effects on the lipid bilayer structure.[16]

Polyunsaturated phospholipids are commonly considered to be able to increase fluidity and permeability of biomembranes. This can cause changes to the function of the cell membrane,[17, 18] as well as affect specific protein and antibody attachment and activity.[18-20] As an example, DHA-phospholipids have been shown to decrease membrane bending rigidity and to favour membrane deformation and fission by dynamin-endophilin complex.[21] These effects can be intuitively ascribed to the folded conformation that polyunsaturated acyl chains assume, which disturbs the lipid packing.[2, 22, 23] However, when the behaviour of lipid bilayers enriched in polyunsaturated lipids is examined in deeper detail, a much more complex mechanism of action is found.

In sphingolipid- and cholesterol-enriched bilayers in the fluid state, DHA-phospholipids are able to induce important changes in the composition and proportion of the “liquid-ordered” (L_o) microdomains (lipid rafts)[24, 25] in equilibrium with “liquid-disordered” (L_d) bilayer regions.[20, 26] Somehow contrary to expectation, the highly flexible and disordered omega-3 fatty acids, especially DHA, increase the molecular order of lipid microdomains.[15] The origin of this effect has been envisaged in their poor affinity for cholesterol because of the multitude of their rapidly changing conformations.[15, 25] As a consequence, DHA-phospholipids tend to segregate into the L_d regions pushing cholesterol into raft regions,[15, 25] which become stiffer.[27] Conversely, enrichment of polyunsaturated chains in L_d regions are thought to result in a higher local disorder. Since the L_d bilayer regions constitute the “continuous sea” in which L_o rafts float, on a large length scale the process is generally associated with an overall increased fluidity of biomembranes.[5, 28, 29] However, the DHA fluidifying ability on L_d lipid bilayer has been recently questioned:[30] differential scanning calorimetry and Laurdan fluorescence have shown that the packing of phospholipids is equally affected by mono- and polyunsaturated acyl chains.[30] Thus, this controversial point deserves further investigation.

Another intriguing aspect of DHA-phospholipid enriched membranes that is not completely understood is their morphological propensity. Brzustowicz *et al.*, in the 2000s, almost incidentally reported that dipolyunsaturated phosphocholine (PC) lipids might form non-bilayer phases.[31] However, their study concerned the phase behaviour of bilayers composed of cholesterol and 1-2-docosahexaenoyl-*sn*-glycero-3-phosphocholine (22:6-22:6PC, Fig. S1A), and no experimental evidence of these non-lamellar structures was shown, apart from a reference to an earlier study performed on binary 22:6-22:6PC/water systems at high temperature.[32] Surprisingly this peculiar behaviour was not further investigated, despite its potential great interest: non-lamellar phases are likely to play a key role in many different biological processes (fusion/fission of the membrane and pore formation,[33] protein recruitment,[34, 35] protein regulation)[35-37].

Overall, these discrepancies and open questions clearly indicate that further research is needed to build a comprehensive understanding of the complex relationships that connect the DHA-phospholipid effects on microscopic features, such as acyl chain order and dynamics within the bilayer, and membrane macroscopic properties, such as morphology.[12, 15, 38]

With the aim at shedding light on this subject, here we investigate, at different scale length, the effects of 22:6-22:6PC on the L_d bilayer formed by the naturally abundant 1-palmitoyl-2-oleyl-*sn*-glycero-3-phosphocholine (POPC) (Fig. S1B). Specifically, we use i.) Neutron Reflectometry (NR), to investigate the mesoscopic organization of the supported lipid bilayer, ii.) Cryogenic Transmission Electron Microscopy (Cryo-TEM), Small Angle Neutron Scattering (SANS) and Dynamic Light Scattering (DLS) to investigate morphological changes of the lipid self-assemblies; iii.) Electron Paramagnetic Resonance (EPR) to analyse the molecular arrangement of the lipids within the aggregates and, specifically, the dynamics of the acyl chains. We investigate systems with low and high 22:6-22:6PC content and show that small amounts of 22:6-22:6PC are able to perturb the bilayer increasing its fluidity and ability to rearrange in multilamellar structures. More interesting, we find that, beyond an omega-3 threshold concentration, the incorporation of 22:6-22:6PC in L_d lipid membranes impairs formation of lamellar phases and induces the formation of small spherical aggregates prone to clusterize, as the likely result of the partial exposure of the acyl chains to the aqueous medium.

We propose that the DHA-phospholipid peculiar tendency to self-aggregate in non-lamellar structures, even in combination with lipids that give L_d phases, and the existence of a 22:6-22:6PC threshold concentration for this transition are the key features of this molecule, which could allow a fine control of membrane properties and membrane associated events.

Results

Mesoscopic organization of supported lipid bilayers containing 22:6-22:6PC

Mesoscopic organization of POPC/22:6-22:6PC membranes supported on a solid silicon surface was investigated by means of neutron reflectivity. In particular, we characterized lipid bilayers with different di-DHA phospholipid contents ($x_{22:6\text{-}22:6PC}$ = 0.2, 0.4 and 0.8, where $x_{22:6\text{-}22:6PC}$ is the 22:6-22:6PC molar fraction with respect to total lipids), as well as pure POPC bilayers for comparison. NR profiles (Figs. 1A and S2) were analysed by using a fitting procedure that employs as input parameters the scattering length densities and molecular volumes of all the chemical components (Table S1), which in our systems are: 1. the silicon support, 2. the silicon oxide layer on which the lipid bilayer is deposited, 3. the thin water layer interposed between the support and the lipid bilayer, 4. the lipid headgroups and 5. the lipid tails, as represented in the sketch in Fig. S3. The fitting is based on parameterized volume fraction profiles of all these components,[39, 40] while the lipid bilayers are modelled as three slabs: two identical slabs corresponding to the headgroup regions sandwiching one single slab corresponding to the tail region (Fig. S3). For each slab, thickness, scattering length density (*SLD*), solvent volume fraction and interfacial roughness were obtained by fitting the experimental NR curves, thus furnishing information about the structural organization of the supported membrane.

NR profiles in D_2O, both experimental data and best fitting curves, are reported in Fig. 1A for all the systems analysed.

View Article Online
DOI: 10.1039/D0SM01540K

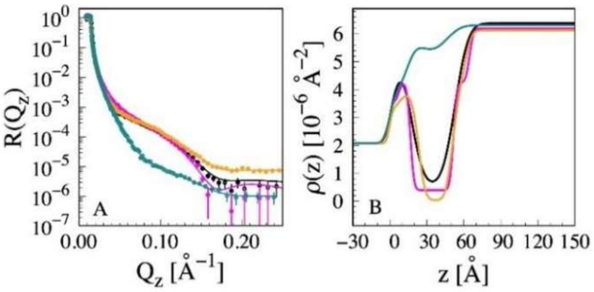

Fig. 1 A) NR profiles and B) *SLD* profiles for pure POPC (black) and POPC/22:6-22:6PC bilayers with $x_{22:6\text{-}22:6PC} = 0.2$ (magenta), POPC/22:6-22:6PC $x_{22:6\text{-}22:6PC} = 0.4$ (orange) and POPC/22:6-22:6PC $x_{22:6\text{-}22:6PC} = 0.8$ (cyan). Measurements performed on the Figaro reflectometer at the ILL (France)[41] and on the INTER reflectometer at ISIS (UK).[42]

It clearly emerges that pure POPC and mixed POPC/22:6-22:6PC bilayers with a low omega-3 content, *i.e.* $x_{22:6\text{-}22:6PC} = 0.2$ and 0.4, are characterized by similar NR profiles, whereas at higher concentration of 22:6-22:6PC a significantly different profile is obtained (Fig. 1A). The same distinction applies to *SLD* profiles derived from fitting (Figs. 1B and S4): for POPC and POPC/22:6-22:6PC bilayers with $x_{22:6\text{-}22:6PC} = 0.2$ and 0.4 *SLD* profiles are very similar to each other and to profiles usually obtained in the case of model supported lipid bilayers,[43-45] while for POPC/22:6-22:6PC $x_{22:6\text{-}22:6PC} = 0.8$ the profile has a completely different shape lacking the deep well visible in the other cases.

A closer look at *SLD* profiles and analysis of parameters derived from fitting (Table 1) show that a low percentage of 22:6-22:6PC causes slight but significant variations of the bilayer features. The POPC bilayer is characterized by a thickness of 29 ± 2 Å in the tail region and of 6 ± 2 Å in the headgroup region, in very good agreement with the literature.[43, 44] In the case of POPC/22:6-22:6PC $x_{22:6\text{-}22:6PC} = 0.2$, a slightly thicker bilayer is observed, with a tail thickness of 34 ± 2 Å and a headgroup thickness of 13 ± 2 Å. By further increasing 22:6-22:6PC content up to $x_{22:6\text{-}22:6PC} = 0.4$, the bilayer becomes thinner in the tail regions while preserving a headgroup thickness not too different from that obtained at $x_{22:6\text{-}22:6PC} = 0.2$. As for the area/lipid, all three values indicate a high coverage of the support.

Table 1 Lipid bilayer structural parameters corresponding to the best fit of Neutron Reflectivity profiles. Errors are calculated by Bootstrap Method.[46]

	Headgroup Thickness [Å]	Tails Thickness [Å]	Roughness σ_{bil} [Å]	Area/ lipid [Å²]
POPC	6±2	29±2	7±3	70±3
POPC/22:6-22:6PC $x_{22:6\text{-}22:6PC}$=0.2	13±2	34±2	3±2	55±4
POPC/22:6-22:6PC $x_{22:6\text{-}22:6PC}$=0.4	10±2	28±2	4±2	62±3
POPC/22:6-22:6PC $x_{22:6\text{-}22:6PC}$=0.8	4±2	20±3	9±2	460±30

As anticipated, for the bilayer with $x_{22:6\text{-}22:6PC} = 0.8$ the NR and *SLD* profiles change dramatically with respect to the other systems (Figs. 1A and B). In particular, the *SLD* profile presents no minimum in the tail region, suggesting a very low surface coverage. This is further supported by the area/lipid value that is one order of magnitude higher than those determined for the other systems (Table 1).

A clear picture of bilayer organization can be obtained looking at convoluted volume fraction distribution profiles (Fig. 2), which describe the distribution of all chemical components moving from the silicon block towards the bulk solvent (deconvoluted volume fraction distribution profiles are reported in Fig. S5). Peaks appearing in these profiles indicate a high-volume occupancy of the considered component. In the case of POPC and the two systems at low omega-3 content, peaks are observed for lipid headgroups at *z* ~ 20 and 60 Å, and for lipid tails at *z* ~ 40 Å, while the water profile reaches a maximum plateau value beyond *z* ~ 70 Å. These results confirm the formation of a lipid bilayer supported by the silicon support (Fig. 2 panels A-C). On the contrary, for POPC/22:6-22:6PC mixtures with $x_{22:6\text{-}22:6PC} = 0.8$, the water volume occupancy becomes very high already at *z* ~ 20-40 Å, in the region where lipid tails were expected (Fig. 2D), while volume occupancies of tails and headgroups are overall very low.

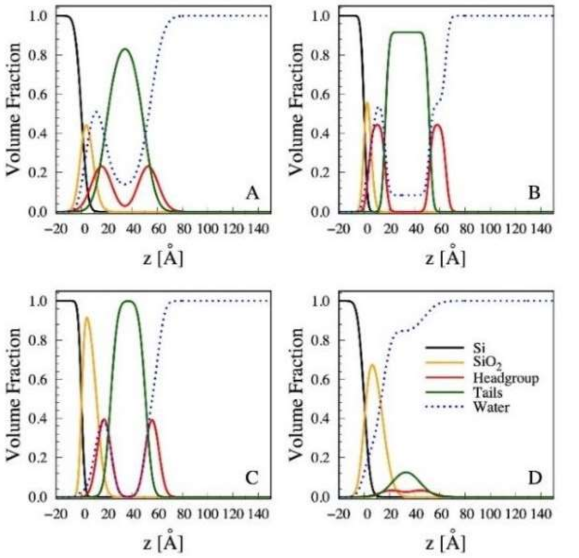

Fig. 2 Convoluted volume fraction distribution profiles for silicon (black), SiO_2 (orange), lipid headgroup (red), lipid tails (green) and water (dashed blue line) for lipid systems: A) POPC, B) POPC/22:6-22:6PC $x_{22:6\text{-}22:6PC} = 0.2$, C) POPC/22:6-22:6PC $x_{22:6\text{-}22:6PC} = 0.4$, D) POPC/22:6-22:6PC $x_{22:6\text{-}22:6PC} = 0.8$, respectively.

All these findings, *i.e.* the unusual *SLD* profile, the very high area/lipid value and the peculiar volume fraction distribution profiles, can be explained as the result of a significant change of the bilayer/support interactions in the case of POPC/22:6-22:6PC lipid mixtures with $x_{22:6\text{-}22:6PC} = 0.8$. This evidence could be hypothesized to derive from a dramatic increase of fluidity associated with a low membrane bending rigidity and a low propensity to adsorb onto the solid still preserving a lamellar lipid organization or possibly resulting by a massive structural reorganization of the lipid supramolecular assembly.

In order to shed light on the causes of this phenomenon, we analysed vesicles of POPC/22:6-22:6PC at different omega-3 content by means of Cryo-TEM, SANS and DLS.

Morphological organization of vesicles containing 22:6-22:6PC

The morphology of lipid aggregates with low ($x_{22:6\text{-}22:6PC} = 0.2$) and high (0.8) 22:6-22:6PC content was investigated by means of Cryo-TEM (Fig. 3). POPC vesicles were also considered for comparison.

View Article Online
DOI: 10.1039/D0SM01540K

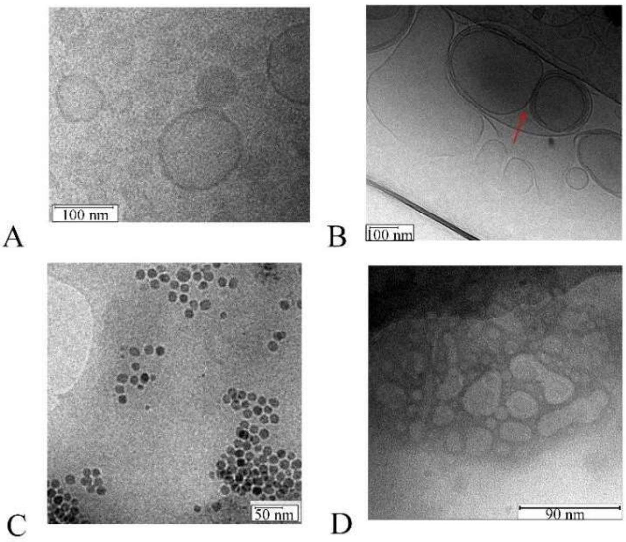

Fig. 3 Cryo-TEM micrographs of POPC (A) and POPC/22:6-22:6PC lipid mixtures with $x_{22:6-22:6PC}$ = 0.2 (B) and 0.8 (C, D). The image in panel B was processed using a band pass filter with Image J program.

Micrographs of the pure POPC system (Fig. 3A) show the presence of unilamellar vesicles, with a mean radius of about 60 nm, together with a few multilamellar structures. In the case of POPC/22:6-22:6PC mixtures with $x_{22:6-22:6PC}$ = 0.2 (Fig. 3B) multilayer and elongated vesicles are observed. In some cases, juxtaposed vesicles present a quite flat contact area (see the arrow in panel B). Overall, these results indicate an increased bilayer flexibility.

In the case of POPC/22:6-22:6PC lipid mixture with $x_{22:6-22:6PC}$ = 0.8, we observe clusters of small spherical particles (Fig. 3C), which coexist with larger structures, looking as blobs with highly polydispersed water-filled cavities (Fig. 3D), while no vesicle is found.

By performing a quantitative analysis of Cryo-TEM images of this system (as an example see Fig. 4A) we determined a mean diameter of about 9 ± 1 nm for the small particles (Fig. 4B) with a polydispersity index of about 1.

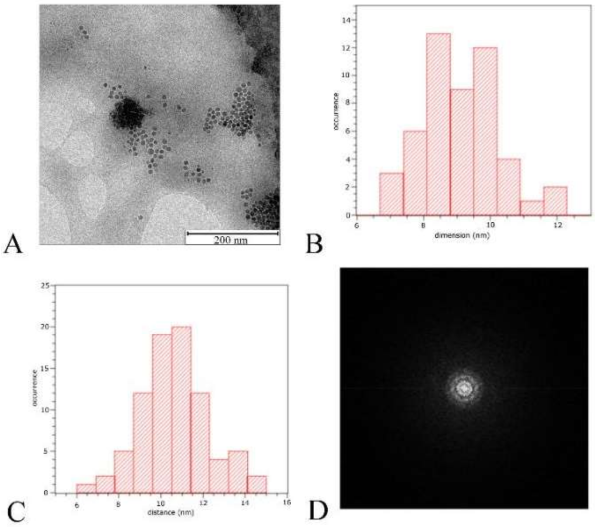

Fig. 4 Cryo-TEM micrograph of the POPC/22:6-22:6PC lipid mixture with $x_{22:6-22:6PC}$ = 0.8 (A), particle diameter distribution (B), interparticle distance distribution (C), fast Fourier transform of particle clusters (D).

Despite an average centre-to-centre interparticle distance of about 11 ± 1 nm (Fig. 4C) indicates a close packing of spherical aggregates within the clusters, fast Fourier transforms of the areas containing these particles (Fig. 4D) rule out the presence of ordered repetitive units. On the other hand, image analysis of blobs (Fig. S6) indicates that, assuming a single quasi-circular shape, the cavities have a mean diameter of 15 ± 6 nm with a polydispersity index of 1.5.

Overall, in the presence of a high concentration of 22:6-22:6PC we do not observe vesicles or ordered lamellar aggregates, indicating that lipid detachment highlighted by NR could be indeed the result of a membrane reorganization.

Aiming at further investigating these lipid arrangements, we performed SANS experiments for POPC/22:6-22:6PC lipid mixtures with $x_{22:6-22:6PC}$ = 0.2, 0.4, 0.8, as well for pure POPC and 22:6-22:6PC.

Inspection of SANS profiles (Fig. 5) highlights that no peak is present in any case. The absence of a peak at high-*q* indicates that the lipid aggregates do not have a repetitive multilamellar structure, with a fixed distance among stacked lamellae, while the absence of a peak at low-*q* indicates that there is no inter-aggregate interaction. SANS profiles for POPC and POPC/22:6-22:6PC $x_{22:6-22:6PC}$ = 0.2 and 0.4 are very similar to each other. In particular, at intermediate *q* values the profiles follow a power law $d\Sigma/d\Omega \propto q^{-\alpha}$ with α >2. On the contrary, in the case of POPC/22:6-22:6PC with $x_{22:6-22:6PC}$ = 0.8 and pure 22:6-22:6PC, the scattering decays as q^{-2}. The q^{-2} slope is a characteristic signature of locally planar surfaces; a higher slope is indicative of the presence of some multilamellar structures.

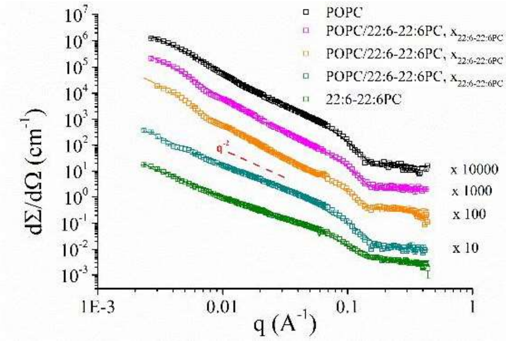

Fig. 5 SANS profiles for pure POPC (black), POPC/22:6-22:6PC mixtures with $x_{22:6-22:6PC}$ = 0.2 (magenta), $x_{22:6-22:6PC}$ = 0.4 (orange), $x_{22:6-22:6PC}$ = 0.8 (cyan) and pure 22:6-22:6PC (green). Experimental data are represented as open squares, while best fitting curves as bold lines. The q^{-2} slope is explicitly shown as a dashed red line. For the sake of clarity, the SANS profiles were shifted by multiplication as indicated in the figure.

A detailed quantitative analysis was performed by fitting the SANS data using the SASView program.[47] In all the cases, no structure factor was taken into account. For what concerns the form factor, we used a lamellar stack paracrystal model,[48] usually employed for treatment of large multilamellar vesicles, for pure POPC and POPC/22:6-22:6PC mixtures with $x_{22:6-22:6PC}$ = 0.2 and 0.4. Fitting gave a similar bilayer thickness of ~35 Å, while the number of layers increases with the omega-3 content (Table 2).

View Article Online
DOI: 10.1039/D0SM01549K

Table 2 – Structural parameters as derived from model fitting of SANS profiles. Errors as derived from fitting are reported.

	Model	Thickness (Å)	*N* layers	⟨*D*⟩ (Å)	*σD*/⟨*D*⟩	Radius (Å)	Polydispersity
POPC	Lamellar stack paracrystal	34.32 ± 0.06	3.316 ± 0.003	65.22 ± 0.06	1.568 ± 0.002	-	0.1 (on thickness)
POPC/22:6-22:6PC $x_{22:6\text{-}22:6PC} = 0.2$	Lamellar stack paracrystal	35.78 ± 0.07	5.470 ± 0.006	64.9 ± 0.4	1.70 ± 0.02	-	0.2 (on thickness)
POPC/22:6-22:6PC $x_{22:6\text{-}22:6PC} = 0.4$	Lamellar stack paracrystal	34.37 ± 0.04	6.246 ± 0.009	66.19 ± 0.04	1.608 ± 0.003		0.2 (on thickness)
POPC/22:6-22:6PC $x_{22:6\text{-}22:6PC} = 0.8$	Vesicles	28.48 ± 0.07	-	-	-	80.21 ± 0.03	0.7 (on radius)
22:6-22:6PC	Vesicles	29.06 ± 0.02	-			78.38 ± 0.02	0.8 (on radius)

In the case of the POPC/22:6-22:6PC mixture with $x_{22:6\text{-}22:6PC} = 0.8$ and pure 22:6-22:6PC, the lower intensity at low q with respect to the other systems, being the concentration the same, points towards the presence of aggregates characterized by a smaller volume. At the same time, the q^{-2} trend (Fig. 5) suggests the presence of lamellar structures. We tried several models to fit the data, including a disk model, but only using the vesicle model we had good results and low χ^2 values. Fit of experimental data according to this model indicates a thickness of ~28 Å and a radius of ~80 Å. The presence of vesicles characterized by these structural parameters should have resulted in some Bragg peaks due to interference between adjacent lamellae, which are not present in the profile. This apparent contradiction could be interpreted as the result of the coexistence of different aggregates: small ones with dimensions not far from those of particles seen in cryo-TEM images and another aggregated form that preserves a lamellar lipid arrangement.

To investigate the coexistence of different aggregates, and possibly shed light on their relative content, we performed Dynamic Light Scattering (DLS) measurements. Indeed DLS, such as SANS, is in principle more sensitive to large objects than to smaller ones, with the intensity proportional to the sixth power of radius; in addition it allows a normalization of the data to be performed, thus converting the intensity-weighted profiles (that can be compared with SANS results) into number-weighted profiles, with intensity proportional to the radius (that can be compared with Cryo-TEM results). The latters give an indication of the concentration of the different species in the sample.

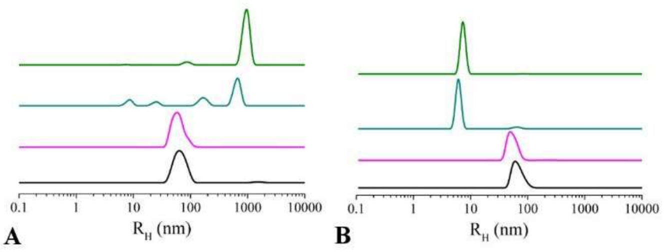

Fig. 6 Intensity-weighted (A) and number-weighted (B) DLS profiles for pure POPC (black), POPC/22:6-22:6PC $x_{22:6\text{-}22:6PC} = 0.2$ (magenta), POPC/22:6-22:6PC $x_{22:6\text{-}22:6PC} = 0.8$ (cyan) and pure 22:6-22:6PC (green).

As reference samples we analysed pure POPC and 22:6-22:6PC and POPC/22:6-22:6PC at low ($x_{22:6\text{-}22:6PC} = 0.2$) and high ($x_{22:6\text{-}22:6PC} = 0.8$) omega-3 content.

In the case of pure POPC and the system at $x_{22:6\text{-}22:6PC} = 0.2$, intensity-weighted DLS profiles (Fig. 6A) show the presence of a single population, centred at about 65 nm. This value of R_H is in good agreement with those usually determined for POPC unilamellar vesicles[49] and the one measured by Cryo-TEM (see above). In the case of pure 22:6-22:6PC and the system with $x_{22:6\text{-}22:6PC} = 0.8$, different populations are visible and the main one is centred at very high R_H values, of the order of hundreds of nm (Table 3). Number-weighted profiles (Fig. 6B) of the first two systems are very similar to intensity-weighted profiles: a single population centred at about the same R_H value as before (Table 3). This is indeed the only species present. When looking at systems with a high 22:6-22:6PC content, a completely different picture arises: now a single population is present centred at much lower R_H values, about 8 nm (Table 3). This value is very close to the radius value determined by SANS as well as to dimension of particles observed in Cryo-TEM images, considering the contribution of the hydration shell to the R_H value.

Table 3 Dimension and relative content of lipid aggregates in systems with different content of 22:6-22:6PC. Errors on R_H are within 5%.

	Intensity-weighed profiles		Number-weighed profiles	
	R_H (nm)	% Intensity	R_H (nm)	% Number
POPC	66	98	60	100
POPC/22:6-22:6PC $x_{22:6\text{-}22:6PC} = 0.2$	64	100	57	100
POPC/22:6-22:6PC $x_{22:6\text{-}22:6PC} = 0.8$	8 25 165 644	9 6 19 66	8	97
22:6-22:6PC	9 87 1008	1 5 94	8	99

Overall, these findings confirm the presence of multiple aggregates in the systems with high content of 22:6-22:6PC and identify small aggregates with radius comparable to that of spherical particles seen by Cryo-TEM as the most abundant ones (Table 3).

Microstructural organization of vesicles containing 22:6-22:6PC

Finally, we investigated the microstructure of POPC/22:6-22:6PC aggregates, as deriving from the local lipid arrangement, by electron paramagnetic spectroscopy. Detailed information was gained using the spin-labelled lipids 5- and 14-PCSL (Fig. S1 C and D),[50] bearing the reporter nitroxide group either close to the headgroup or in proximity of the apolar terminus, respectively. Lipid mixtures in the whole $0 \leq x_{22:6\text{-}22:6PC} \leq 1$ range were considered, namely POPC/22:6-

View Article Online
DOI: 10.1039/D0SM01549K

22:6PC systems with $x_{22:6\text{-}22:6PC}$ = 0.2, 0.4, 0.6, 0.8, as well as pure POPC and pure 22:6:22:6PC.

The spectra (Fig. S7) were analysed by computer simulation of the EPR lineshape (Figs S8-9), extracting the following main parameters: (a) the hyperfine coupling constant <*A*>, which is related to the polarity experienced by the paramagnetic label; (b) the correlation time for the label rotational motion *τ*, which is related to the local microviscosity; (c) the order parameter *S*, a measure of the orientational ordering of the labelled segment of the acyl chain with respect to the normal to the bilayer surface. It has to be highlighted that for no spin-label and at no lipid mixture composition we observed the superposition of EPR signals, which could have been indicative of a spin-label partitioning in two different aggregate types. Taking that EPR spectroscopy furnishes number-weighted results, we can assume that data reported below refer to the lipid aggregates present in the higher percent (by number, as observed by DLS analysis)

The parameters obtained from the simulations of 14-PCSL spectra are shown in Fig. 7A as a function of 22:6-22:6PC content. Below $x_{22:6\text{-}22:6PC}$ = 0.4, <*A*> and *S* remain nearly constant, indicating the structural organization of the bilayer to be scarcely affected by the presence of polyunsaturated lipids. In this composition range, only *τ* shows a significant variation: its decrease points to bilayers with a more fluid interior. Above $x_{22:6\text{-}22:6PC}$ = 0.4, *S* and *τ* present an abrupt decrease, indicating that the lipid self-organization becomes much less tight and more dynamic. Particularly, the acyl chain termini are free to move and assume different orientations. The parallel increase of <*A*> indicates that they are exposed to a more polar environment. Indeed, <*A*> assumes values typical of labels positioned at the aggregate interface.[44, 45]

Even in the case of 5-PCSL, <*A*> and *S* do not change in the low $x_{22:6\text{-}22:6PC}$ range, while *τ* weakly decreases (Fig. 7B). Above $x_{22:6\text{-}22:6PC}$ = 0.4 *S* and *τ* decrease, even though to a lesser extent with respect to the variations observed for 14-PCSL. Both parameters assume almost constant values above $x_{22:6\text{-}22:6PC}$ = 0.7. For 5-PCSL, <*A*> remains almost constant in the whole bilayer composition range.

Thus, both spin-labels confirm that inclusion of 22:6-22:6PC in the lipid mixture above the threshold lipid concentration of $x_{22:6\text{-}22:6PC}$ = 0.4 causes a rearrangement of the local lipid self-organization, corresponding to the changes observed by NR, SANS and DLS. Moreover, from a microscopic viewpoint, the EPR results indicate that the polyunsaturated lipid differently perturbs the acyl chain self-organization depending on the distance from the headgroup.

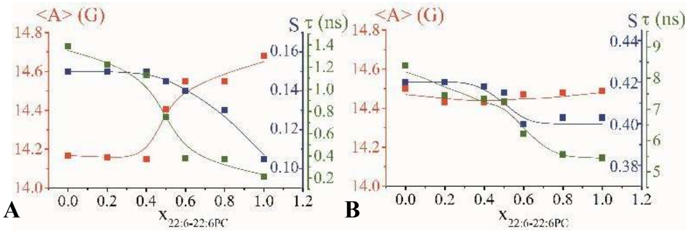

Fig. 7 Order parameter *S* (blue), hyperfine coupling constant <*A*> (red) and correlation time *τ* (green) of 14-PCSL (A) and 5-PCSL (B) included in POPC/22:6-22:6PC lipid mixtures, as a function of the 22:6-22:6PC fraction.

Integration of these results with those obtained using other two spin-labels, namely 7-PCSL and 10-PCSL, furnishes the complete profile of the local structuring and micropolarity experienced by the lipid acyl chain segments. This analysis was performed on the lipid mixtures that are well below ($x_{22:6\text{-}22:6PC}$ = 0.2) and above ($x_{22:6\text{-}22:6PC}$ = 0.8) the transition range, as well as on pure POPC for comparison. The three *S* profiles (Fig. 8) highlight a marked difference between the pure POPC and the $x_{22:6\text{-}22:6PC}$ = 0.2 systems on one side and the $x_{22:6\text{-}22:6PC}$ = 0.8 system on the other side. In particular, the former flexibility profiles are characteristic hallmark of the disordered state of liquid-crystalline phospholipid bilayers, L_d,[51] with the *S* value obtained for 10-PCSL close to those relative to 5-PCSL and 7-PCSL and a steep decrease for 14-PCSL. The lipid mixture with $x_{22:6\text{-}22:6PC}$ = 0.2 presents only a small reduction of the order parameter for all spin-labels. These results point to a slight enhancement of the bilayer fluidity, as also confirmed by the correlation times (Table S2).

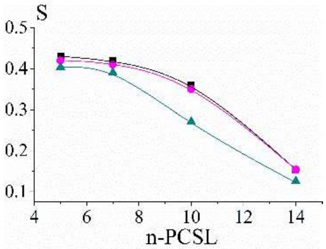

Fig. 8 Order parameter *S* as a function of the spin label position, n-PCSL, for pure POPC (black), POPC/22:6-22:6PC $x_{22:6\text{-}22:6PC}$ = 0.2 (magenta) and POPC/22:6-22:6PC $x_{22:6\text{-}22:6PC}$ = 0.8 (cyan).

In the case of $x_{22:6\text{-}22:6PC}$ = 0.8, a strong reduction is observed specifically for 10-PCSL, indicating a dramatic decrease of the ordering of the middle segments of the acyl chains.[52]

Discussion

Our investigation shows that 22:6-22:6PC, a lipid presenting two polyunsaturated acyl chains, when inserted in liquid disordered membranes, such as those formed by POPC, affects their features in a content-dependent manner. Up to a composition of about $x_{22:6\text{-}22:6PC}$ = 0.4, results obtained by different experimental techniques indicate that 22:6-22:6PC does not alter the membrane morphology: NR indicates the presence of supported lipid bilayers, while SANS and Cryo-TEM show the presence of multilamellar vesicles, similar to those formed by pure POPC. However, from a microscopic viewpoint, 22:6-22:6PC induces an increase of acyl chain mobility freedom, as clearly highlighted by the τ trends obtained by EPR (Fig. 7). Moreover, a slight ordering decrease is observed in the *S* profile of $x_{22:6\text{-}22:6PC}$ = 0.2 system (Fig. 8). This relatively modest microscopic perturbation of the acyl chain self-organization reflects in a slightly but still detectable increase of the bilayer deformability as suggested by Cryo-TEM images (Fig 3B) and in the ability to rearrange, forming vesicles with higher multilamellarity, as well-shown by results of SANS data fitting (Table 2).

At higher concentrations, 22:6-22:6PC effects do not limit to a membrane flexibility increase, and, beyond the $x_{22:6\text{-}22:6PC}$ = 0.4 threshold, it induces a marked reorganization of the lipid supramolecular aggregates. NR results show that a supported lipid bilayer is no longer present at $x_{22:6\text{-}22:6PC}$ = 0.8, and lipid detachment occurs. In corresponding Cryo-TEM micrographs, we observe a massive membrane reorganization, leading to phase separation and coexistence of two different kinds of aggregates, none of them vesicular: small spherical particles and large blobs with water-filled cavities. This massive structural rearrangement is likely to be the cause of lipid detachment observed in NR experiments. It is worth to stress that despite the hydrophobic mismatch between POPC and 22:6-22:6PC in no case we observe formation of bicelles by means of Cryo-TEM or SANS, as found in the case of other mixture of saturated and unsaturated lipids.[53, 54] This may be due to the fact that POPC itself contains an unsaturated chain or to the high conformational flexibility of 22:6-22:6PC hydrophobic tails that might allow them to adapt to different aggregate geometries. It is possible that the two lipids differently distributes between the two aggregate types. However, we have no means to quantify this partitioning.

For what concerns the bigger aggregates, they can be described as very large assemblies, with dimensions of the order of hundreds of nanometres according to DLS, with irregular shapes and water filled cavities (Fig. 3D). As for lipid arrangement, SANS data suggest they preserve a lamellar organization. Formation of not vesicular and not localized bounded structures with a lamellar arrangement of lipids was observed in other cases; for example, Schneider *et al.* described a network-like structure that forms as a consequence of enhanced membrane elasticity in a limited temperature range.[55] In the present case, the increased aggregate flexibility and elasticity due to the omega-3 presence may represent the driving force for this structural rearrangement. Our data show no evidence of domain formation, as a result of lipid segregation within the aggregate. However, we cannot exclude this phenomenon, whose occurrence is well-established in the presence of cholesterol.[56]

We were able to achieve a deeper characterization of the small aggregates that according to DLS number-weighted profiles are the most abundant species. Cryo-TEM and SANS show that they are small spherical particles, with a radius of about 7-8 nm, a value very close to that determined by DLS too. Moreover, analysis of Cryo-TEM micrographs highlights their tendency to cluster. Because of their abundance, we can confidently assume that microstructural characterization by EPR refers to them. EPR results prove that beyond the $x_{22:6\text{-}22:6PC} = 0.4$ threshold, concurrently with the phase separation, a structural transition occurs, as clearly pointed out by the strong discontinuity in the 14PCSL *<A>* and *S* profiles. In particular, we observe a transition from the lipid organization typical of the L_d phase formed by pure POPC to a structural arrangement in which the lipid tails are more disordered and freer to move. In more details, EPR shows that the whole lipid chain is affected by this transition, but changes are particularly evident for the chain terminus, which presents a much higher rotational dynamics, as highlighted by the τ decrease observed for 14-PCSL, and can bend, strongly deviating from the parallelism to the normal to the aggregate surface, as revealed by the *S* drop. Consequently, chain termini can insert among the headgroups and come in contact with the external aqueous medium. This can be clearly inferred from the 14-PCSL *<A>* values, which assume values similar to, and even higher than, those observed for 5-PCSL (see Fig 7). Further insights are deducible from analysis of the *S* profile (Fig. 8). Hardman *et al.*, when working with 1-palmitoyl-2-*sn*-oleyl-glycero-phosphoethanolamine (POPE), associated a profile very similar to that we found for $x_{22:6\text{-}22:6PC} = 0.8$ system to a non-lamellar structure, specifically the inverted hexagonal phase, H_{II},[57] proposed also for 18:0-22:6PE,[58] on the bases of ^{31}P-NMR. However, Fourier transform performed on regions of cryo-TEM images containing these small aggregates rules out the possible presence of H_{II} phases in our systems, suggesting that this supramolecular lipid organization is selectively favoured by phosphoethanolamine moieties, while being hindered by the bulkier phosphocholine headgroups. Interestingly, in a recent work concerning inverted structures such as lipid stabilized W/O nanoemulsions, we found low *S* values for the intermediate chain segments.[52] This resembles the dramatic *S* decrease in position 10 observed in samples at high 22:6-22:6PC content. Thus, even in the absence of a regular (liquid crystalline) arrangement of the lipid aggregates, the observed *S* trend can be confidently interpreted has a hallmark of the formation of structures in which the chain termini are not constrained in the aggregate interior but point toward the aggregate surface. Overall, the EPR results indicate that the lipids tend to assume disordered conformations within the small aggregates; specifically, the acyl chains can fold exposing both the headgroup and the tail termini. This explains why the small spherical structures shown by cryo-TEM images tend to cluster, but still present a water layer between them.

It is worth to note that Dekker *et al.* observed aggregates characterized by a fast motion in all directions by means of ^{31}P NMR in the case of binary solutions water/22:6-22:6PC at temperatures higher than 60 °C whereas at lower temperatures these systems formed lamellar phases.[32] Our findings indicate that indeed small aggregates are formed by 22:6-22:6PC even in combination with POPC and at room temperature. Moreover, our results indicate that a minority portion of the 22:6-22:6PC rich samples indeed preserve a lamellar arrangement of lipids even if they are not in a vesicular form. The apparent discrepancy concerning the aggregation behaviour of 22:6-22:6PC at room temperature may be related to the different conditions used (use of PBS in the place of Tris/acetate buffer and NaCl 0.1 M or the addition of hydrochinone to lipid samples)[32] since the presence of salts and additives can strongly affect lipid aggregation behaviour.

Our study well highlights the strict interconnection between changes in conformational order of the acyl chains, on a molecular/ microscopic length scale, and shape/dimension/deformability variations of the supramolecular aggregates, on a mesoscopic length scale. Although seemingly different, these different viewpoints on lipid phase transitions are related since both of them are coupled to thermodynamic fluctuations in the membrane properties.[55]

Overall morphological and microstructural characterization of lipid mixtures with a high content of 22:6-22:6PC indicates that this lipid is able to induce a marked reorganization of the lipid bilayer, resulting in a phase separation into two different types of aggregates, of which the most abundant are small spherical aggregates largely exposing hydrophobic tails as in inverted micelles. We suggest that the peculiar aggregation properties of 22:6-22:6PC lipids may have a role in determining biological roles of omega-3: they can facilitate formation of transient non-bilayer structures, where a reorganization with negative curvature into the inner hydrophobic region occurs.[12, 59]

Furthermore these 22:6-22:6PC abilities also support the rational exploitation of polyunsaturated lipids in drug carrier formulations (including nanoemulsions,[60] vesicles, cubosomes, sponge-type particles),[61] as evidenced by the numerous patents released in the last years. Specifically, these lipids could be proposed as the strategic components of cargo particles able to target specific tissues (*e.g.*, the brain),[62] where they could be rapidly incorporated in the plasma membrane, effectively releasing the active to be delivered.

Experimental

Materials

Dichloromethane, methanol and ethanol (HPLC-grade purity) were purchased from Merck (Darmstadt, Germany); D_2O (99% purity) and Phosphate Buffer Saline (PBS) tabs from Sigma Aldrich (St. Louis, MO). 1-Palmitoyl-2-oleoyl-*sn*-glycero-3-phosphatidylcholine (POPC) 1,2-didocosahexaenoyl-*sn*-glycero-3-phosphocholine (22:6-22:6PC) and spin-labeled phosphatidylcholines (1-palmitoyl-2-stearoyl-(n-doxyl)-*sn*-glycero-3-phosphocholine, n-PCSL) with the nitroxide group in the positions 5, 7, 10 and 14 of the acyl chain, were purchased from Avanti Polar Lipids (Birmingham, AL, USA). Molecular structures of the lipids used in this study are shown in Fig. S1

Sample preparation

Samples containing POPC and different amounts of 22:6-22:6PC were prepared by mixing appropriate amounts of lipids, dissolved in a dichloromethane–methanol mixture (2:1 v/v, 10 mg/mL lipid concentration), in a round-bottom test tube. For Electron Paramagnetic Resonance measurements spin-labeled phosphatidylcholines (n-PCSL) were added to the lipid mixture (1 % by mole on the total lipids) by mixing appropriate amounts of a spin-label solution in ethanol (1 mg/mL) with the lipid organic mixture.

A thin lipid film was formed by evaporating the solvents with dry nitrogen gas, and then final traces of solvents were removed by subjecting the sample to vacuum desiccation for at least 3 h. The samples were finally hydrated with PBS solution in water, pH=7.4, thus obtaining 1 mM multi lamellar vesicle (MLV) suspensions. These samples were directly used for EPR measurements. For Cryo-TEM, SANS and DLS experiments, MLV suspensions were repeatedly extruded through a 100 nm pore size polycarbonate membrane to obtain large unilamellar vesicles (LUVs). All the samples were monitored for at least 24 h, no change being detected.

Neutron reflectometry measurements were performed on lipid bilayers deposited on monocrystalline silicon supports through the vesicle fusion protocol. For this purpose, a 0.5 mM vesicle suspension was injected in the solid-liquid reflectometry flow cell and equilibrated with the silicon support surface for 30 min. Then pure D_2O was injected into the cell, leading to the rupture of the vesicles and formation of the desired planar lipid bilayers.

Control for lipid breakdown

Omega-3 breakdown is initiated by free-radical formation and subsequent propagation of a chain-reaction that proceeds autocatalytically. In order to minimize 22:6-22:6PC breakdown, in our protocol we reduced factors such as oxygen, light and iron ions. All physical handling of lipids was performed in an inert atmosphere under low light conditions. All solvents and buffers were deoxygenated by bubbling with inert gas in order to remove dissolved oxygen. Moreover, the extent of lipid breakdown was assessed by UV spectroscopic assay: indeed lipids with no conjugated double bonds give a single strong absorption peak at ~200 nm, while breakdown-induced conjugation results in a strong peak at 235 nm; the ratio of peak heights at 235 and 200 nm allows lipid breakdown to be monitored. In no case we observed degradation of lipids employed in our study.

View Article Online
DOI: 10.1039/D0SM01549K

Neutron reflectivity (NR)

Neutron reflectivity measurements were performed on the FIGARO reflectometer [63] at the high flux reactor of the Institut Laue-Langevin (ILL, Grenoble, France) in time-of-flight mode using a spread of wavelengths between 2 and 20 Å with two incoming angles of 0.8 and 3.2° (doi:10.5291/ILL-DATA.8-02-703), with the only exception of measurements for the POPC/22:6-22:6PC $x_{22:6\text{-}22:6PC}$=0.4 systems that were performed on the high-flux neutron reflectometer INTER[42] at ISIS Facility, Science and Technology Facilities Council (Didcot, UK) using neutron wavelengths from 1.5 to 16 Å with two incident angles of 0.7°and 2.3°.

The specular reflection at the silicon/water interface, *R,* defined as the ratio between the reflected and the incoming intensities of a neutron beam, is measured as a function of the wave vector transfer, *q*, perpendicular to the reflecting surface. *R(q)* is related to the scattering length density (*SLD*) across the interface, $\rho(z)$, which depends on the composition of the adsorbed species. The neutron scattering length density, $\rho(z)$, is defined by the following relation:

$$\rho(z) = \sum_j n_j(z) b_j \qquad (1)$$

where $n_j(z)$ is the number of nuclei per unit volume and b_j is the scattering length of nucleus *j*. The scattering lengths of the constituent fragments of any species adsorbed at the surface are the fundamental quantities from which the interfacial properties and microstructural information on the lipid bilayer are derived. Measurement of the same system in different solvent contrasts greatly enhances the sensitivity of the technique.[64] Samples were measured using H_2O, SMW (silicon-matched water), 4MW and D_2O as solvent contrasts. SMW (ρ = 2.07 × 10^{-6} Å^{-2}) is a mixture of 38 vol % D_2O (ρ = 6.35 × 10^{-6} Å^{-2}) and 62 vol % H_2O (ρ = -0.56 × 10^{-6} Å^{-2}) with the same refraction index for neutrons as a bulk silicon, while 4MW (ρ = 4 × 10^{-6} Å^{-2}) consists of 66 vol % D_2O and 34 vol % H_2O (Fig. S2).

Analysis of NR profiles

Neutron Reflectivity curves were analysed with a fitting procedure based on parameterized volume fraction profiles of all chemical components (silicon, silicon oxide, water, lipid tails and headgroups) as detailed below. The method has been validated by previous works.[39, 40]

Distribution Function

To model our data, we assumed a water/silicon (W/Si) interface, of roughness σ_{int}, modelled with two error functions

$$\Phi^0_{Si}(z) = \frac{1}{2}\cdot\left[1 - erf\left(\frac{z}{\sqrt{2}\sigma_{int}}\right)\right] \qquad (6)$$

$$\Phi^0_{Wat}(z) = \frac{1}{2}\cdot\left[1 - erf\left(\frac{-z}{\sqrt{2}\sigma_{int}}\right)\right] \qquad (7)$$

where z denotes the distance to the interface and σ_{int} the interfacial roughness of a bare W/Si interface. Nevertheless, in the presence of lipids or silicon oxide, just the unoccupied volume is filled up with water, as described below:

View Article Online
DOI: 10.1039/D0SM01549K

$$\Phi_{Wat}(z) = \frac{1}{2}\cdot(1-\Phi_{occ}(z))\cdot\left[1-erf\left(\frac{-z}{\sqrt{2}\sigma_{int}}\right)\right] = \Phi^{0}_{Wat}(z)\cdot(1-\Phi_{occ}(z)) \qquad (8)$$

Subsequently, volume distribution profile of silicon oxide (SiO_2) is modelled as a slab function. The slab function is defined as the difference between two error functions:

$$\Phi(z) = \frac{1}{2}\phi\cdot\left[erf\left(\frac{z-z_0+d/2}{\sqrt{2}\sigma_l}\right) - erf\left(\frac{z-z_0-d/2}{\sqrt{2}\sigma_r}\right)\right] \qquad (9)$$

where ϕ and d represent the volume fraction and the thickness, σ_l and σ_r are adjustable parameters specifying the roughness of the layer towards the silicon substrate and the water respectively. The parameter z_0 represents the distribution centre which can be offset with respect to the W/Si interface ($z = 0$).

The lipid bilayer was modelled as three slabs: two identical slabs corresponding to the two head regions sandwiching one single slab corresponding to the tail region. Head and tail components respect the physical molar constraint expected for a lipid bilayer such that:

$$\int_{-\infty}^{+\infty}\Phi_{tail}(z)dz = \frac{v_{tail}}{v_{head}}\int_{-\infty}^{+\infty}\Phi_{head}(z)dz \qquad (10)$$

where v_{head}, v_{tail} are the headgroup and tail molecular volumes (see Table S1) respectively and $\Phi_{head}(z)$, $\Phi_{tail}(z)$ are their volume fraction distributions as a function of z as described in Eq. 6.

It is important to specify that in the presence of 22:6-22:6PC, headgroup and tail physical parameters (*i.e.* molecular volume and *SLD*) are calculated by mixing values reported in Table S1 with the suited mol/mol ratio ($x_{22:6\text{-}22:6PC}$ =0, 0.2, 0.4 or 0.8).

a. Interfacial and Bilayer Roughness: convolution integral

In order to describe the z profile distribution of all chemical components in the system, a further step considering the interfacial roughness as a global parameter is required.

By assuming that adsorption of lipids at the W/Si interface depends on the interaction between the two, the purpose of the volume fraction profile modelling is to provide a model considering the interface as flat. In fact, the interfacial roughness becomes relevant when radiation is reflected and refracted which, if interfacial roughness is properly taken into account, results in a feature smearing effect. In addition, one more parameter representing the global roughness (or the waviness) of the bilayer σ_{bil} is introduced.

The two roughening effects described above have been taken into account during the modelling process, as follows:

i) a set of parameters is generated;

ii) Distribution profiles $\Phi_{Si}(z)$, $\Phi_{Wat}(z)$, $\Phi_{SiO_2}(z)$, $\Phi_{head}(z)$, $\Phi_{tail}(z)$ are calculated by assuming $\sigma_{int} = 0$ and $\sigma_{bil} = 0$;

iii) $\Phi_{head}(z)$, $\Phi_{tail}(z)$ are convoluted by a Gaussian function of width σ_{bil} as follows:

$$\Phi^{bil}_{head,tail}(z) = \frac{1}{\sqrt{2\pi}\sigma_{bil}}\int_{-\infty}^{+\infty}\Phi_{head,tail}(\zeta)\cdot e^{-\frac{(z-\zeta)^2}{2\sigma_{bil}^2}}d\zeta \qquad (11)$$

where $\Phi^{bil}_{head,tail}(z)$ represents the convoluted distribution profile corresponding to headgroup and tails of the lipid bilayer;

iv) $\Phi^{bil}_{head,tail}(z)$ and $\Phi_{SiO_2}(z)$ are convoluted by a Gaussian function of width σ_{int} as follows:

$$\Phi^{int}_{head,tail}(z) = \frac{1}{\sqrt{2\pi}\sigma_{int}}\int_{-\infty}^{+\infty}\Phi^{bil}_{head,tail}(\zeta)\cdot e^{-\frac{(z-\zeta)^2}{2\sigma_{int}^2}}d\zeta \qquad (12)$$

$$\Phi^{int}_{SiO_2}(z) = \frac{1}{\sqrt{2\pi}\sigma_{int}}\int_{-\infty}^{+\infty}\Phi_{SiO_2}(\zeta)\cdot e^{-\frac{(z-\zeta)^2}{2\sigma_{int}^2}}d\zeta \qquad (13)$$

v) $\Phi_{occ}(z)$ is calculated as the sum of volume distribution profiles of silicon oxide and lipids:

$$\Phi_{occ}(z) = \Phi^{int}_{head,tail}(z) + \Phi^{int}_{SiO_2}(z) \qquad (14)$$

vi) eventually the volume fraction profiles of silicon substrate and water, $\Phi^{0}_{Si}(z)$, $\Phi_{Wat}(z)$ are calculated by using Eq. 6 and Eq. 8 respectively.

b. Surface Excess

Volume fraction distributions can be used for calculating the surface excess of lipids adsorbed onto the W/Si interface. This quantity represents the lipids adsorbed per unit area. Mathematically it can be calculated as follows:

$$\Gamma_{lipid} = \frac{v_{lipid}}{\int_{-\infty}^{+\infty}\Phi_{lipid}(z)dz} \qquad (15)$$

with M_{lipid} and v_{lipid} molar weight and molecular volume of the lipid mixtures used in this work (see Table S1).

c. SLD profiles

With all the volume fraction profiles resolved the corresponding *SLD* profiles, $\rho(z)$ are then calculated as:

$$\rho(z) = \rho_{Si}(z)\cdot\Phi^{0}_{Si}(z) + \rho_{SiO_2}(z)\cdot\Phi^{int}_{SiO_2}(z) + \rho_{Wat}(z)\cdot\Phi_{Wat}(z) + \rho_{head}(z)\cdot\Phi^{int}_{head}(z) + \rho_{tail}(z)\cdot\Phi^{int}_{tail}(z) \qquad (16)$$

where $\rho_i(z)$ represents the *SLD* value of the corresponding chemical component, as reported in Table S1.

Discretized *SLD* profiles in 1 Å thick slices are then used for calculation of the corresponding reflectivity curves $R(Q_z)$ by using Parratt recursive algorithm.[65] At this step, due to the discretized *SLD* profiles, roughness between adjacent layers is set to zero.

d. Penalty Function χ^2

Reflectivity curves obtained as described above can be compared with experimental data. If N_d experimental reflectivity curve $R^{exp}(Q_z)$ are taken into account, each of them with n experimental points for which we can calculate a model reflectivity curve $R^{mod}(Q_z)$, we can define a penalty function χ^2 as follows:

$$\chi_k^2(\Lambda_k) = \frac{1}{\mu - \nu - \sum_{i=1}^{N_d} n_i} \sum_{i=1}^{N_d} \sum_{j=1}^{n_i} \frac{\left(R^{exp}(Q_z) - R^{mod}(Q_z)\right)^2}{\epsilon_{i,j}^2} \qquad (17)$$

with n_i the number of experimental points for the i-th dataset. Λ_k, ν and μ represent the set of parameters, the number of free parameters and the number of constraints respectively.

The penalty function described above is used during the fitting procedure for evaluating the best model with the lowest χ^2 value.

Cryogenic transmission electron microscopy (cryo-TEM)

Cryogenic transmission electron microscopy (cryo-TEM) images were carried out at the Heinz Maier-Leibnitz Zentrum, Garching, Germany on a JEOL 200 kV JEM-FS2200 with a field emission gun (FEG). Samples for TEM were prepared by placing a drop of the 0.5 mg/mL solution on a Quantifoil Multi A carbon-coated copper grid. After a few seconds, excess solution was removed by blotting with filter paper.

The sample was cryo-fixed by rapid immersing into liquid ethane at 93 K in a cryo-plunge (EMGP Leica GmbH). The specimen was inserted into a cryo-transfer holder (HTTC 910, Gatan, Munich, Germany) and transferred to a JEM 2200 FS EFTEM instrument (JEOL, Tokyo, Japan). Examinations were carried out at temperatures around 93 K. The transmission electron microscope was operated at an acceleration voltage of 200 kV. Zero-loss filtered images were taken under reduced dose conditions (<10 000 e^-/nm^2). All images were recorded digitally by a bottom-mounted 16-bit CMOS camera system (TemCam-F216, TVIPS, Munich, Germany). To avoid any saturation of the grey values, all the measurements were taken with intensity below 15 000, considering that the maximum value for a 16-bit camera is 2^16. Images have been taken with EMenu 4.0 image acquisition program (TVIPS, Munich, Germany) and processed with a free digital imaging processing system Image J.[66-68] We used EMenu 4.0 program also to perform manual measurement of the particle and vesicles diameters, as well as measurement of inter-particle distances. The statistical characteristics of the particles, namely the number-average diameter (D_n), the weight-average diameter (D_w), and the polydispersity index (*PDI*), were calculated using the following equations:[69]

$$D_n = \frac{\Sigma d_i}{n} \qquad (2)$$

$$D_W = \frac{\Sigma (d_i)^4}{\Sigma (d_i)^3} \qquad (3)$$

$$PDI = \frac{D_W}{D_n} \qquad (4)$$

where d_i represents the diameters of the microspheres, and *n* is the number of particles.

Finally, we calculated the power spectra from the original images and radial averaged the produced transformed images with the EMenu 4.0 program.

View Article Online
DOI: 10.1039/D0SM01549K

Small Angle Neutron Scattering

Small Angle Neutron Scattering (SANS) measurements were performed at 25 °C with the KWS-1 diffractometer operated by the Jülich Centre for Neutron Science (JCNS) at the FRMII source located at the Heinz Maier Leibnitz Centre, Garching (Germany).[70, 71] For all the samples, neutrons with a wavelength of 5 Å and $\Delta\lambda/\lambda \leq 0.1$ were used. A two-dimensional array detector at three different wavelength (W)/collimation (C)/sample-to-detector (D) distance combinations (W 5 Å/C 8 m/D 2 m, W 5 Å/C 8 m/D 8 m, and W 5 Å/C 20 m/ D 20 m) measured neutrons scattered from the samples. The scattering intensity was collected in the range of the modulus of the scattering vector $q = 4\pi n \sin(\vartheta/2)/\lambda$, between 0.0023 Å^{-1} and 0.45 Å^{-1}. Here λ and ϑ represents the wavelength of the neutron beam and scattering angle respectively. All the samples were dissolved in D_2O at 1 mM total lipid concentration. Each sample and solvent background was placed in capped 2 mm path length quartz cuvettes, in order to prevent solvent evaporation and exchange with atmospheric water vapour.

Analysis of SANS data

The raw data were corrected for background and empty cell scattering. Detector efficiency correction, radial average and transformation to absolute scattering cross sections $d\Sigma/d\Omega$ were made with a secondary plexiglass standard. The absolute scattering cross section data $d\Sigma/d\Omega$ were plotted as function of *q*. The dependence of $d\Sigma/d\Omega$ from the scattering vector can summarized as:

$$\frac{d\Sigma}{d\Omega} = n_p P(q) S(q) + \left(\frac{d\Sigma}{d\Omega}\right)_{incoh} \qquad (5)$$

where n_p is the number of scattering objects, *P(q)* and *S(q)* are respectively the form factor and the structure factor. The last term takes into account the incoherent scattering mostly due to the presence of hydrogen atoms within the sample. Structural information can be extrapolated by choosing an appropriate model to fit the experimental data. So a detailed quantitative analysis was performed by fitting the data using the SASView program.[47] In all the cases, no structure factor was taken into account. For what concerns the form factor, we used a lamellar stack paracrystal model,[48] usually employed for treatment of large multilamellar vesicles, for pure POPC and POPC/22:6-22:6PC with $x_{22:6\text{-}22:6PC} = 0.2$ and 0.4 systems, and a vesicle model for POPC/22:6-22:6PC with $x_{22:6\text{-}22:6PC} = 0.8$ and pure 22:6-22:6PC. A Shultz polydispersity of the thickness was taken into account in the case of the lamellar stack paracrystal model, while a Schultz polydispersity of the radius was taken into account for the vesicle model.

In the case of the lamellar stack paracrystal model the scattering intensity *I(q)* was calculated as

$$I(q) = 2\pi \Delta\rho^2 \Gamma_m \frac{P_{bil}(q)}{q^2} Z_N(q) \qquad (18)$$

where $\Delta\rho$ is the contrast, Γ_m is the volume fraction of the material in the bilayer, P_{bil} is the form factor of the bilayer and it is approximated as the cross section of an infinite, planar bilayer of thickness *t* according to

View Article Online
DOI: 10.1039/D0SM01549K

$$P_{bil}(q) = \left(\frac{sin\left({}^{qt}/_{2}\right)}{{}^{qt}/_{2}}\right)^{2} \qquad (19)$$

Finally, $Z_N(q)$ describes the interference effects for aggregates consisting of more than one bilayer, and depends on the number of bilayers N, the average distance between adjacent layers $\langle D\rangle$ and the relative standard deviation of the Gaussian layer distance distribution $\sigma D/\langle D\rangle$.

The form factor of the vesicle is

$$P(q) = \frac{\Phi}{V_{shell}}\left[\frac{3V_{core}\ (\rho_{solvent} - \rho_{hell})j_1(qR_{core})}{qR_{core}} + \frac{3V_{tot}(\rho_{shell} - \rho_{solvent})j_1(qR_{tot})}{qR_{tot}}\right]^2 + bkg \qquad (20)$$

where Φ is the volume fraction of shell material, V_{shell} is the volume of the shell, V_{core} is the volume of the core, V_{tot} is the total volume, R_{core} is the radius of the core, R_{tot} is the outer radius of the shell, $\rho_{solvent}$ is the scattering length density of the solvent (which is the same as for the core in this case), ρ_{shell} is the scattering length density of the shell, bkg is a flat background level (due for example to incoherent scattering in the case of neutrons), and j_1 is the spherical Bessel function.

Dynamic Light Scattering (DLS)

Dynamic Light Scattering (DLS) measurements were performed by using a home-made instrument composed by a Photocor compact goniometer, a SMD 6000 Laser Quantum 50 mW light source operating at 532.5 nm, a photomultiplier (PMT-120-OP/B) and a correlator (Flex02-01D) from *Correlator.com*. All measurements were performed at 25 °C with the temperature controlled through thermostatic bath and at $\theta = 90$ °. All the samples were dissolved in PBS at 1 mM total lipid concentration.

Electron Paramagnetic Resonance (EPR) Spectroscopy

EPR spectra were recorded with a 9 GHz Bruker Elexys E-500 spectrometer (Bruker, Rheinstetten, Germany). The capillaries containing MLVs suspensions were placed in a standard 4 mm quartz sample tube containing light silicone oil for thermal stability. All the measurements were performed at 25 °C. Spectra were recorded using the following instrumental settings: sweep width, 100 G; resolution, 1024 points; time constant, 20.48 ms; modulation frequency, 100 kHz; modulation amplitude, 1.0 G; incident power, 6.37 mW. Several scans, at least 8, were accumulated to improve the signal-to-noise ratio.

Analysis of EPR data

The spectra (Fig. S7) were analysed by computer simulation of the EPR lineshape (Figs. S8-9) using the well-established procedure by Budil *et al*.[72,73-75] The g_{ii} values for the coupling between the electron spin and the magnetic field were chosen in order to have the best fitting for all spectra and were g_{ii}=2.0075, 2.006, 2.003. In some cases, due to fitting improvements, 2.0027 was used instead of 2.003 for g_{zz}.

The computation allowed us to extract the following main parameters: (a) the A_{ii} main components of the A tensor for the hyperfine coupling between the unpaired electron spin and the nitrogen nuclear spin; (b) the correlation time for the rotational motion τ; (c) the order parameter S.

For what concerns the A_{ii} values, we maintained constant A_{xx}=7.1 G and A_{yy}=7.2 G values, which well fitted all the spectra, while it was needed to change the A_{zz} value from one system to another as summarized in Tables S2-3, where we list the $<A>=(A_{xx}+A_{yy}+A_{zz})/3$ values. For what concerns the correlation time, it was necessary to include in the calculation an anisotropy of motion, also considering a tilt of the rotational axis, but, for simplicity, we took constant both the $\tau_{//}$ value (13.2 ns, indicative of the steric hindrance of the chain in its parallel direction with respect to the p-orbital hosting the unpaired electron) and the tilt angle (70°). Therefore, the main parameter changing from one to another system is the perpendicular value of the correlation time for motion, simply indicated as τ and reported both in Figs. S8-9 and Table S2-3.

Conclusions

The microscopic and mesoscopic structural characterization of bilayers formed by POPC and an increasing content of 22:6-22:6PC indicates that the general fluidifying effect reported up to now for L_d phases in the presence of omega-3 fatty acids is a very partial picture of the whole lipid mixture behaviour. At low 22:6-22:6PC concentrations, only a slight increase of lipid dynamics is indeed observed, but this increase although small is sufficient to determine structural changes on a larger scale, such as membrane deformability and higher multilamellarity. At higher concentrations, the large-scale structural reorganization becomes noticeable: vesicles are no longer present, a minor part of the system preserves a lamellar lipid arrangement but in large irregular shapes, coexisting with clusters of small spherical aggregates. Formation of these species is related to a significant conformational change on a microscopic scale: thanks to the presence of multiple unsaturations, lipid chains tend to fold by exposing the hydrophobic tails to the solvent in close vicinity with the hydrophilic headgroups.

The finding that the omega-3 phospholipid 22:6-22:6PC strongly disfavours the formation of lamellar phases and induces assembly in non-lamellar structures not only provides a reasonable key to interpret many different physico-chemical properties of polyunsaturated lipids, but also opens a new pathway towards a comprehension of their biological role. Although molar fractions of 22:6-22:6PC above the threshold of 0.4 total lipids could appear as excessively high concentrations, one should bear in mind that this lipid was proved to segregate with respect to other lipids forming rafts, so that high local concentrations of 22:6-22:6PC could indeed be present in membranes in the L_d mesophase. In these conditions, it could play a fundamental role in regulating membrane associated events, facilitating reorganization with negative curvature into the inner hydrophobic region, essential for membrane fusion and fission processes, as well as formation of transient non-bilayer structures involved also in protein interaction. This could be the case of neural and synaptic membranes, where polyunsaturated lipids seem to somehow respond to the need of efficient membrane vesiculation,[21] and preferentially interact with amyloidogenic peptides.[76]

In the general framework of the revised concept of the fluid mosaic model,[77] based on the paradigm of a lipid diversity-phase polymorphism, a great research interest is direct towards those lipids that may have different roles: (a) favour the insertion of proteins into the membrane and tune their activities; (b) regulate signalling and respond to stress conditions; and, last but not least, (c) facilitate membrane fusion/fission, by promoting the formation of non-lamellar phases, which both theoretical and experimental data indicate to exist, at least transiently, *in vivo*.[78-80] Our results indicate that omega-3 lipids are perfect candidates to meet these requirements.

Conflicts of interest

There are no conflicts to declare.

Acknowledgements

This work is based upon experiments performed at the FIGARO instrument operated by the ILL, Grenoble, France (doi:10.5291/ILL-DATA.8-02-703, 10.5291/ILL-DATA.8-02-801), at the KWS-1 instrument operated by JCNS at the Heinz Maier-Leibnitz Zentrum (MLZ), Garching, Germany and at the INTER reflectometer operated at the ISIS Facility, Science and Technology Facilities Council (Didcot, UK). The authors are thankful for the award of beamtime and use of the facilities. This work benefited from the use of the SasView application, originally developed under NSF Award DMR-0520547. SasView also contains code developed with funding from the EU Horizon 2020 programme under the SINE2020 project Grant No 654000.

Authors' contribution

ADS: Validation, Formal analysis, Investigation, Writing-original draft, Visualization; GV: Investigation; MSA: Formal analysis, Investigation; ES: Formal analysis, Writing-original draft, Visualization; GF: Investigation; LCB: Investigation; LC: Investigation; MFO: Formal analysis, Writing-original draft; LP: Validation, Formal analysis, Investigation; IRK: Conceptualization, Methodology, Validation, Formal analysis, Writing-original draft, Writing-Review & Editing, Visualization, Supervision, Project administration; GDE: Conceptualization, Methodology, Validation, Formal analysis, Writing-original draft, Writing-Review & Editing, Visualization, Supervision, Project administration, Funding acquisition

References

1. D. R. Robinson, L. L. Xu, S. Tateno, M. Guo and R. B. Colvin, *J Lipid Res*, 1993, **34**, 1435-1444.
2. C. Lor and L. S. Hirst, *Membranes*, 2015, **5**, 857-874.
3. S. C. Cunnane, R. Chouinard-Watkins, C. A. Castellano and P. Barberger-Gateau, *Prostag Leukotr Ess*, 2013, **88**, 61-70.
4. S. M. Innis, *J Nutr*, 2007, **137**, 855-859.
5. B. Antonny, S. Vanni, H. Shindou and T. Ferreira, *Trends Cell Biol*, 2015, **25**, 427-436.
6. K. Gawrisch, O. Soubias and M. Mihailescu, *Prostag Leukotr Ess*, 2008, **79**, 131-134.
7. P. C. Calder, *Ann Nutr Metab*, 2016, **69 Suppl 1**, 7-21.
8. M. J. Weiser, C. M. Butt and M. H. Mohajeri, *Nutrients*, 2016, **8**, 99.
9. M. V. Bell, J. R. Dick and C. Buda, *Lipids*, 1997, **32**, 1085-1091.
10. G. P. Miljanich, L. A. Sklar, D. L. White and E. A. Dratz, *Biochim Biophys Acta*, 1979, **552**, 294-306.
11. M. I. Aveldano, *Colloq Inse*, 1989, **195**, 87-96.
12. W. Stillwell and S. R. Wassall, *Chem Phys Lipids*, 2003, **126**, 1-27.
13. R. P. Bazinet and S. Laye, *Nat Rev Neurosci*, 2014, **15**, 771-785.
14. S. Laye, *Prostag Leukotr Ess*, 2010, **82**, 295-303.
15. S. R. Shaikh, J. J. Kinnun, X. Leng, J. A. Williams and S. R. Wassall, *Biochim Biophys Acta-Biomemb*, 2015, **1848**, 211-219.
16. M. Pinot, S. Vanni, S. Pagnotta, S. Lacas-Gervais, L. A. Payet, T. Ferreira, R. Gautier, B. Goud, B. Antonny and H. Barelli, *Science*, 2014, **345**, 693-697.
17. A. Dickey and R. Faller, *Biophys J*, 2008, **95**, 2636-2646.
18. K. R. Flynn, A. Sutti, L. L. Martin, M. Leigh Ackland and A. A. J. Torriero, *Biochim Biophys Acta-Biomemb*, 2018, **1860**, 1135-1142.
19. H. Barelli and B. Antonny, *Curr Opin Cell Biol*, 2016, **41**, 25-32.
20. W. Stillwell, S. R. Shaikh, M. Zerouga, R. Siddiqui and S. R. Wassall, *Repr Nutr Devel*, 2005, **45**, 559-579.
21. M. M. Manni, M. L. Tiberti, S. Pagnotta, H. Barelli, R. Gautier and B. Antonny, *eLife*, 2018, **7**.
22. R. P. Mason, R. F. Jacob, S. Shrivastava, S. C. R. Sherratt and A. Chattopadhyay, *Biochim Biophys Acta-Biomemb*, 2016, **1858**, 3131-3140.
23. S. C. R. Sherratt and R. P. Mason, *Chem Phys Lipids*, 2018, **212**, 73-79.
24. S. R. Wassall and W. Stillwell, *Chem Phys Lipids*, 2008, **153**, 57-63.
25. S. R. Wassall and W. Stillwell, *Biochim Biophys Acta-Biomemb*, 2009, **1788**, 24-32.
26. S. R. Shaikh, A. C. Dumaual, A. Castillo, D. LoCascio, R. A. Siddiqui, W. Stillwell and S. R. Wassall, *Biophys J*, 2004, **87**, 1752-1766.
27. M. Ibarguren, D. J. Lopez, J. A. Encinar, J. M. Gonzalez-Ros, X. Busquets and P. V. Escriba, *Biochim Biophys Acta-Biomemb,* 2013, **1828**, 2553-2563.
28. W. Ehringer, D. Belcher, S. R. Wassall and W. Stillwell, *Chem Phys Lipids*, 1990, **54**, 79-88.
29. R. C. Valentine and D. L. Valentine, *Progr Lipid Res*, 2004, **43**, 383-402.
30. A. De Santis, Y. Varela, J. Sot, G. D'Errico, F. M. Goni and A. Alonso, *Sci Rep*, 2018, **8**, 16240.
31. M. R. Brzustowicz, V. Cherezov, M. Zerouga, M. Caffrey, W. Stillwell and S. R. Wassall, *Biochem*, 2002, **41**, 12509-12519.
32. C. J. Dekker, W. S. Geurts van Kessel, J. P. Klomp, J. Pieters and B. De Kruijff, *Chem Phys Lipids*, 1983, **33**, 93-106.
33. R. J. C. Gilbert, *Biochim Biophys Acta-Biomemb*, 2016, **1858**, 487-499.
34. M. Ibarguren, D. J. Lopez and P. V. Escriba, *Biochim Biophys Acta-Biomemb*, 2014, **1838**, 1518-1528.
35. P. V. Escriba, X. Busquets, J. Inokuchi, G. Balogh, Z. Torok, I. Horvath, J. L. Harwood and L. Vigh, *Progr Lipid Res*, 2015, **59**, 38-53.
36. J. Martinez, O. Vogler, J. Casas, F. Barcelo, R. Alemany, J. Prades, T. Nagy, C. Baamonde, P. G. Kasprzyk, S. Teres, C. Saus and P. V. Escriba, *Mol Pharmacol*, 2005, **67**, 531-540.
37. P. V. Escriba, M. Sastre and J. A. Garciasevilla, *P Natl Acad Sci USA*, 1995, **92**, 7595-7599.
38. F. X. Contreras, L. Sanchez-Magraner, A. Alonso and F. M. Goni, *FEBS letters*, 2010, **584**, 1779-1786.
39. F. Lolicato, L. Joly, H. Martinez-Seara, G. Fragneto, E. Scoppola, F. B. Bombelli, I. Vattulainen, J. Akola and M. Maccarini, *Small*, 2019, **15**.
40. E. Scoppola, S. Micciulla, L. Kuhrts, A. Maestro, R. A. Campbell, O. V. Konovalov, G. Fragneto and E. Schneck, *Molecules*, 2019, **24**.
41. R. Cubitt and G. Fragneto, *Appl Phys A*, 2002, **74**, s329-s331.
42. J. Webster, S. Holt and R. Dalgliesh, *Physica B: Cond Matt*, 2006, **385-386**, 1164-1166.
43. A. Merlino, G. Vitiello, M. Grimaldi, F. Sica, E. Busi, R. Basosi, A. M. D'Ursi, G. Fragneto, L. Paduano and G. D'Errico, *J Phys Chem B*, 2012, **116**, 401-412.
44. G. Vitiello, A. Falanga, A. A. Petruk, A. Merlino, G. Fragneto, L. Paduano, S. Galdiero and G. D'Errico, *Soft Matter*, 2015, **11**, 3003-3016.
45. G. Vitiello, G. Fragneto, A. A. Petruk, A. Falanga, S. Galdiero, A. M. D'Ursi, A. Merlino and G. D'Errico, *Soft Matter*, 2013, **9**, 6442-6456.
46. B. Efron, in *Breakthroughs in Statistics*, eds. S. Kotz and N. L. Johnson, Springer, New York, 1992, vol. II, pp. 569-593.
47. M. e. a. Doucet, 2019, DOI: 10.5281/zenodo.2652478.
48. M. Kotlarchyk and S. M. Ritzau, *J Appl Crystallogr*, 1991, **24**, 753-758.
49. F. Bianchini, A. De Santis, E. Portioli, I. R. Krauss, L. Battistini, C. Curti, S. Peppicelli, L. Calorini, G. D'Errico, F. Zanardi and A. Sartori, *Nanomed-Nanotechnol*, 2019, **18**, 135-145.
50. M. B. Sankaram, D. Marsh and T. E. Thompson, *Biophys J*, 1992, **63**, 340-349.
51. W. L. Hubbell and H. M. McConnell, *J Am Chem Soc*, 1971, **93**, 314-326.
52. C. Caianiello, M. D'Avino, D. Cavasso, L. Paduano and G. D'Errico, *Nanomat-Basel*, 2020, **10**, 1185.
53. Y. Jiang, H. Wang and J. T. Kindt, *Biophys J*, 2010, **98**, 2895-2903.

View Article Online
DOI: 10.1039/D0SM01549K

54. M. N. Triba, P. F. Devaux and D. E. Warschawski, *Biophys J*, 2006, **91**, 1357-1367.
55. M. F. Schneider, D. Marsh, W. Jahn, B. Kloesgen and T. Heimburg, *Proc Natl Acad Sci U S A*, 1999, **96**, 14312-14317.
56. X. Lin, J. H. Lorent, A. D. Skinkle, K. R. Levental, M. N. Waxham, A. A. Gorfe and I. Levental, *J Phys Chem B*, 2016, **120**, 11930-11941.
57. P. D. Hardman, *Eur J Biochem*, 1982, **124**, 95-101.
58. S. R. Shaikh, M. R. Brzustowicz, W. Stillwell and S. R. Wassall, *Biochem Biophys Res Comm*, 2001, **286**, 758-763.
59. M. Hashimoto, S. Hossain, A. Al Mamun, K. Matsuzaki and H. Arai, *Crit Rev Biotechnol*, 2017, **37**, 579-597.
60. A. A. Esperon-Rojas, R. Baeza-Jimenez and H. S. Garcia, *Biocatal Biotransfor*, 2019.
61. A. Angelova, M. Drechsler, V. M. Garamus and B. Angelov, *ACS Omega*, 2018, **3**, 3235-3247.
62. R. Chouinard-Watkins, R. J. S. Lacombe, A. H. Metherel, M. Masoodi and R. P. Bazinet, *Mol Nutr Food Res*, 2019, **63**.
63. R. A. Campbell, H. P. Wacklin, I. Sutton, R. Cubitt and G. Fragneto, *Eur Phys J Plus*, 2011, **126**.
64. G. Fragneto, R. K. Thomas, A. R. Rennie and J. Penfold, *Langmuir*, 1996, **12**, 6036-6043.
65. L. G. Parratt, *Phys Rev*, 1954, **95**, 359-369.
66. C. A. Schneider, W. S. Rasband and K. W. Eliceiri, *Nat Methods*, 2012, **9**, 671-675.
67. W. S. Rasband, 1997-2012, http://imagej.nih.gov/ij/.
68. M. D. Abramoff, P. J. Magalhaes and S. J. Ram, *Biophotonics Intern*, 2004, **11**, 36-42.
69. G. Q. Pan, B. Y. Zu, X. Z. Guo, Y. Zhang, C. X. Li and H. Q. Zhang, *Polymer*, 2009, **50**, 2819-2825.
70. A. V. Feoktystov, H. Frielinghaus, Z. Y. Di, S. Jaksch, V. Pipich, M. S. Appavou, E. Babcock, R. Hanslik, R. Engels, G. Kemmerling, H. Kleines, A. Ioffe, D. Richter and T. Bruckel, *J Appl Crystallogr*, 2015, **48**, 61-70.
71. H. Frielinghaus, A. Feoktystov, I. Berts and G. Mangiapia, *J Large-scale Res Fac*, 2015, **1**, A28.
72. D. E. Budil, S. Lee, S. Saxena and J. H. Freed, *J Magn Reson Ser A*, 1996, **120**, 155-189.
73. L. Bitan-Cherbakovsky, D. Libster, M. F. Ottaviani, A. Aserin and N. Garti, *J Phys Chem B*, 2012, **116**, 2420-2429.
74. S. Rozner, A. Kogan, S. Mehta, P. Somasundaran, A. Aserin, N. Garti and M. F. Ottaviani, *J Phys Chem B*, 2009, **113**, 700-707.
75. S. Santeusanio, O. A. Attanasi, R. Majer, M. Cangiotti, A. Fattori and M. F. Ottaviani, *Langmuir*, 2013, **29**, 11118-11126.
76. A. Emendato, R. Spadaccini, A. De Santis, R. Guerrini, G. D'Errico and D. Picone, *FEBS letters*, 2016, **590**, 582-591.
77. F. M. Goni, *Biochim Biophys Acta-Biomemb*, 2014, **1838**, 1467-1476.
78. S. Aeffner, T. Reusch, B. Weinhausen and T. Salditt, *Proc Natl Acad Sci U S A*, 2012, **109**, E1609-1618.
79. P. V. Bashkirov, S. A. Akimov, A. I. Evseev, S. L. Schmid, J. Zimmerberg and V. A. Frolov, *Cell*, 2008, **135**, 1276-1286.
80. S. Qian and H. W. Huang, *Biophys J*, 2012, **102**, 48-55.

View Article Online
DOI: 10.1039/D0SM01549K

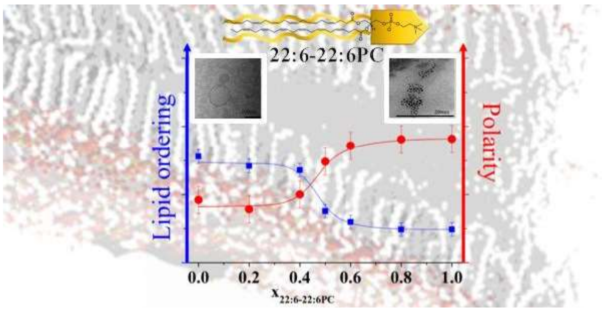

Beyond a threshold concentration, omega-3 phospholipid 22:6-22:6PC hampers formation of the typical lamellar phase of lipid membranes forming small spherical aggregates